A Simulation of the Abyssal Circulation in the North Pacific Ocean. Part II: Theoretical Rationale

HIROSHI ISHIZAKI

Oceanographic Research Department, Meteorological Research Institute, Tsukuba, Japan

(Manuscript received 29 June 1992, in final form 14 January 1994)

ABSTRACT

A theoretical rationale is given for the simulated abyssal circulation in the North Pacific detailed in Part I. A simple theory clarifies the importance of the vertical change in area of the horizontal cross section of the basin owing to the existence of bottom topography, or basin shape. With general upward vertical transport in the basin, a water column horizontally diverges and vertically shrinks as it rises in spite of the general upwelling, resulting in the tendency to produce an anticyclonic circulation. This hypsometric effect is detailed by Rhines and MacCready. In the present case, this effect is present in the lower deep layer (3250–4250 m) and in the bottom layer (below 4250 m) of the North Pacific. In the lower deep layer, a single anticyclonic circulation owing to this effect appears explicitly. In the bottom layer, however, this effect almost balances the cyclogenesis owing to the bottom water influx, resulting in essentially eastward interior flow. On the other hand, an anticyclonic gyre in the upper deep layer (1750–3250 m) is maintained by the vertical shrinking of the water column owing to the outflux from the North to the South Pacific, resulting in a reversed pattern of the Stommel–Arons circulation.

1. Introduction

In the first part of this work (Ishizaki 1994, hereafter referred to as Part I), a detailed description is given of the simulation of the abyssal circulation in the North Pacific. Comparison of the simulation results with recent observations revealed that, although some discrepancies exist, there is a general similarity between them.

Here, a simple theoretical rationale is given to explain the simulated abyssal circulation and to see how the Stommel–Arons theory for the flat-bottom circulation (Part I, Fig. 1) is modified by the introduction of bottom relief or basin shape. The key point is the vertical change in the horizontal cross-sectional area of the basin. With general upward vertical transport in a bowl-shaped basin, a water column horizontally diverges and vertically shrinks as it rises, which tends to produce an anticyclonic circulation. This effect was discussed by Rhines and MacCready (1989) for f-plane dynamics and named the "hypsometric effect."

In the following, a complete description of the present model and experiment is given in section 2. Large-scale features of the simulated abyssal circulation detailed in Part I are briefly repeated in section 3. In section 4, the hypsometric effect is introduced to explain the simulation results. Discussion is given of a balance between two competitive effects on the water column stretching or shrinking: the hypsometry and the lateral influx–outflux. Finally, section 5 is devoted to conclusions. A detailed explanation of some modeling techniques, including a new definition of the equation of state, is found in the appendices.

2. Model description

The numerical model here was developed by the author based on Bryan (1969). The primitive equations of motion in the spherical coordinates are used with the Boussinesq, rigid-lid, and hydrostatic approximations. The internal and external modes of motion are calculated separately. The latter is obtained by solving the vertically averaged vorticity equation. Potential temperature θ and salinity S are independent variables, and density ρ is determined by θ, S, and pressure P through an equation of state newly defined in the present work and described in appendix A.

The model domain (Fig. 1) encompasses the entire Pacific over 134° latitude (70°S–64°N) and 170° longitude (120°E–70°W). The horizontal resolution is 1° in latitude and 1.25° in longitude, with 20 levels in the vertical and 500-m resolution below 2000 m (Table 1). The bottom depth reaches 5750 m, with the deepest level at 5500 m. At the southwestern part of the domain, the South American continent is superposed on the Australian continent to apply a zonally cyclic boundary condition (70°–56°S). The bottom topography around the Drake Passage is smoothly translated

Corresponding author address: Hiroshi Ishizaki, Oceanographic Research Department, Meteorological Research Institute, 1-1 Nagamine, Tsukuba, Ibaraki-ken, 305 Japan.

to that off Australia with a transition width of 6.25° longitude (135°–141.25°E).

The model bottom topography is based on the 5′ × 5′ depth data published by the National Oceanographic Data Center (NODC). First, the original data are simply averaged on the model grid area and then subjectively modified based on the bottom depth chart (GEBCO, Smith and Mammerickx 1980). The subjective modification process is necessary to maintain, for example, the height of seamount chains, which partition basins, and the depth of narrow passages (Fig. 1). Ten islands are included in the domain (Fig. 3 of Part I). Place names north of 30°S are found in Fig. 2 of Part I.

The surface boundary conditions are as follows: the annual-mean temperature and salinity data of Levitus (1982) are used with a 20-day relaxation time along with annual-mean wind stress data of Hellerman and Rosenstein (1983). At the southern boundary (70°S) the same Levitus data are used with the same recovering time from surface to bottom. A no-flux condition for θ and S is used at other lateral boundaries and the bottom boundary. A no-slip condition is used for momentum at all lateral boundaries. The bottom stress works against the lowermost velocity with a rotation of 10° based on the bottom Ekman layer theory (Semtner and Mintz 1977).

TABLE 1. Depths of vertical levels at which potential temperature, salinity, and velocity are defined.

Number	Depth (m)	Number	Depth (m)
1	10	11	1170
2	30	12	1530
3	60	13	2000
4	100	14	2500
5	160	15	3000
6	240	16	3500
7	350	17	4000
8	490	18	4500
9	670	19	5000
10	890	20	5500

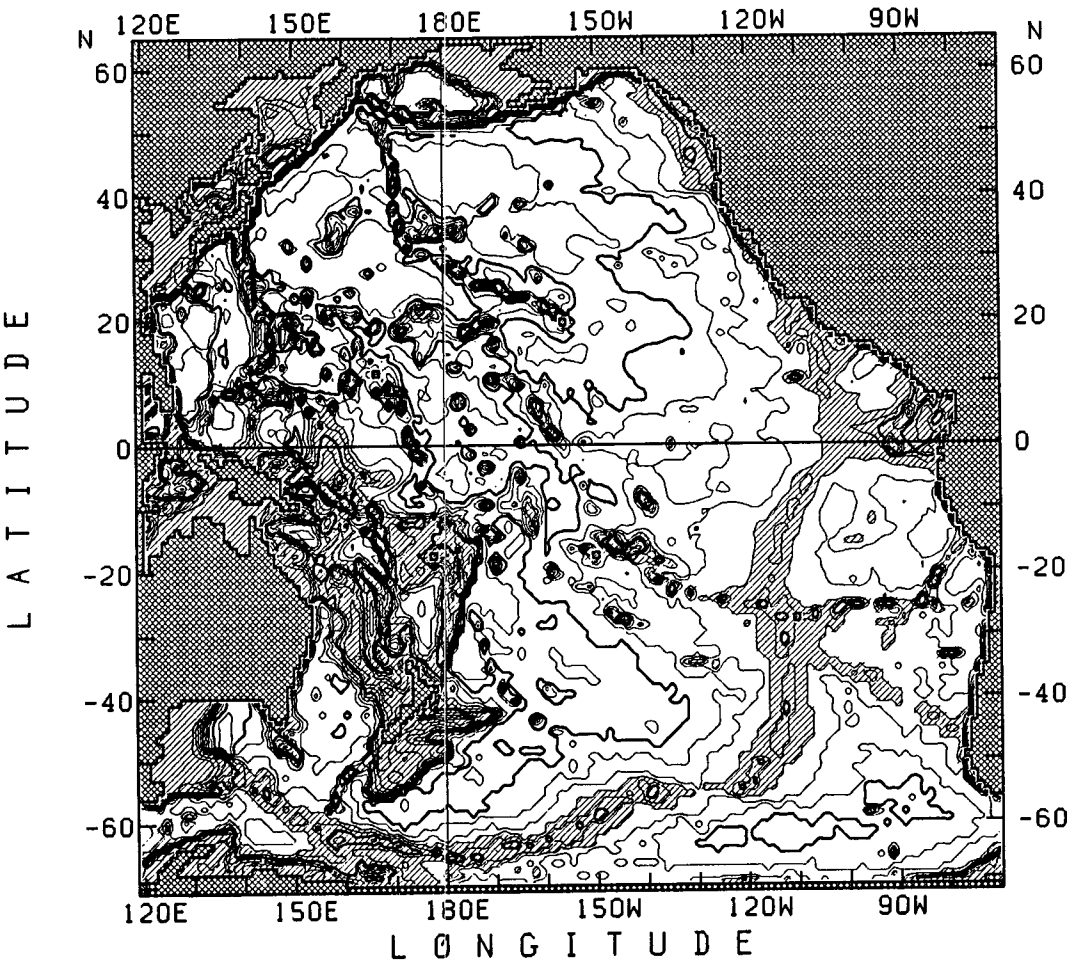

FIG. 1. Model domain with bottom depth contours. Contour interval is 500 m and regions with depths shallower than 3500 m are shaded. See text for an explanation of the topography of the southwestern part of the domain.

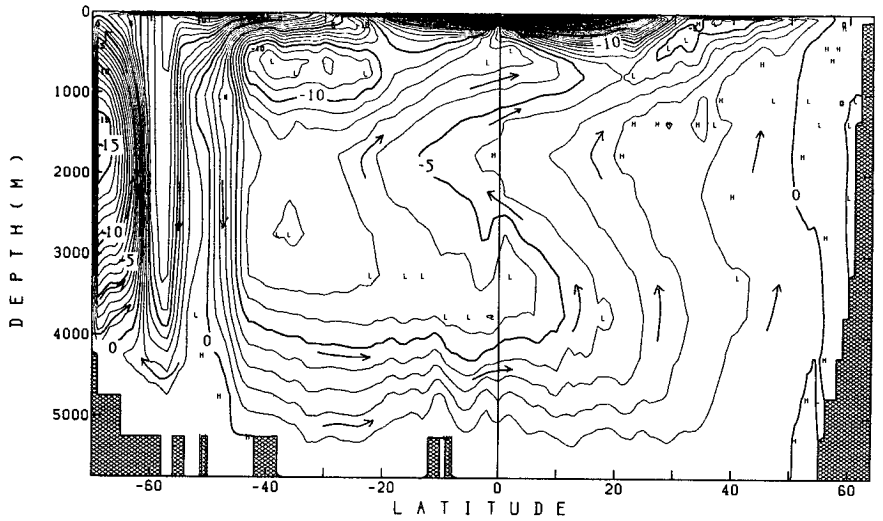

FIG. 2. Zonally integrated meridional circulation. Contour interval is 10^6 m^3 s^{-1} (1 Sv). Arrows indicate flow direction.

The horizontal and vertical eddy viscosity coefficients A_H and A_V are 1×10^8 cm^2 s^{-1} and 10 cm^2 s^{-1} and those for diffusion K_H and K_V are 1×10^7 cm^2 s^{-1} and 0.3 cm^2 s^{-1}, respectively. In the region of the Antarctic Circumpolar Current (ACC), however, the larger value of $K_H = 5 \times 10^7$ cm^2 s^{-1} is used to suppress baroclinic instability.

The horizontal-mean values of θ and S of the Levitus data are taken as initial conditions with a state of rest. The accelerated time integration method of Bryan (1984) is used. The total integration time for layers deeper than 2000 m is about 1000 years. In the first 900 years the model bottom depths were set at the depths of layer boundaries. In this scheme a gentle slope whose declination is much smaller than the ratio of the vertical and the horizontal grid interval cannot be suitably expressed (i.e., wide flat bottoms and cliffs here and there with the same height as the vertical grid interval). In these regions the vertical velocity is concentrated at the cliffs, resulting in relatively strong horizontal currents. To avoid this we modified the scheme at the 900th year to permit an arbitrary model depth at each grid point north of 25°S, so that the thickness of the lowermost layer at each horizontal grid point was variable. The integration was continued for another 100 years. Local flow structures changed after the modification, but the large-scale density and flow fields did not change.

The pressure field is not prognostically predicted but can be diagnostically calculated from the flow and density fields (Semtner and Mintz 1977). It is a powerful indicator of geostrophic horizontal circulations except in equatorial regions. As described in section 3 of Part I, we use it as well as the flow vector field to show horizontal circulations.

Further explanation of numerical techniques used in the present experiment can be found in appendix B.

3. Results

Figure 2 indicates zonally integrated meridional overturning and Fig. 3 shows horizontal circulation patterns at three levels, 2500, 3500, and 5000 m, determined by the pressure field (reproduced from Part I). North of 50°S a large single thermohaline cell is dominant in the abyssal layer below 2000 m over both hemispheres (Fig. 2). About 6.5 Sv (Sv $\equiv 10^6$ m^3 s^{-1}) of bottom water enters the North Pacific as a northward abyssal flow in the layer below 3500 m. Of the 6.5 Sv, 2.8 Sv returns to the South Pacific in the layer between 3250 m and 1750 m. The remaining 3.7 Sv water ascends through the 1750-m level in the entire North Pacific.

The large-scale flow in the bottom layer below 4250 m (Fig. 3c) is essentially zonal and eastward except for the western boundary current region and the Philippine Sea. The bottom western boundary current flows northward without any stagnation point at the western boundary, contrary to the prediction of Stommel and Arons (1960) (Fig. 1 of Part I). Interior flows are generally eastward, going up the gentle slope of the western flank of the East Pacific Rise. The highest-pressure region in the North Pacific is at low latitudes, reflecting the geostrophic balance.

In the lower deep layer between 4250 m and 3250 m (Fig. 3b), the circulation pattern is completely different from that below. A single anticyclonic gyre dominates the entire North Pacific except the Philippine Sea. The region with high pressure is at middle latitudes, although its center is divided by seamount chains. The northward western boundary flow and the

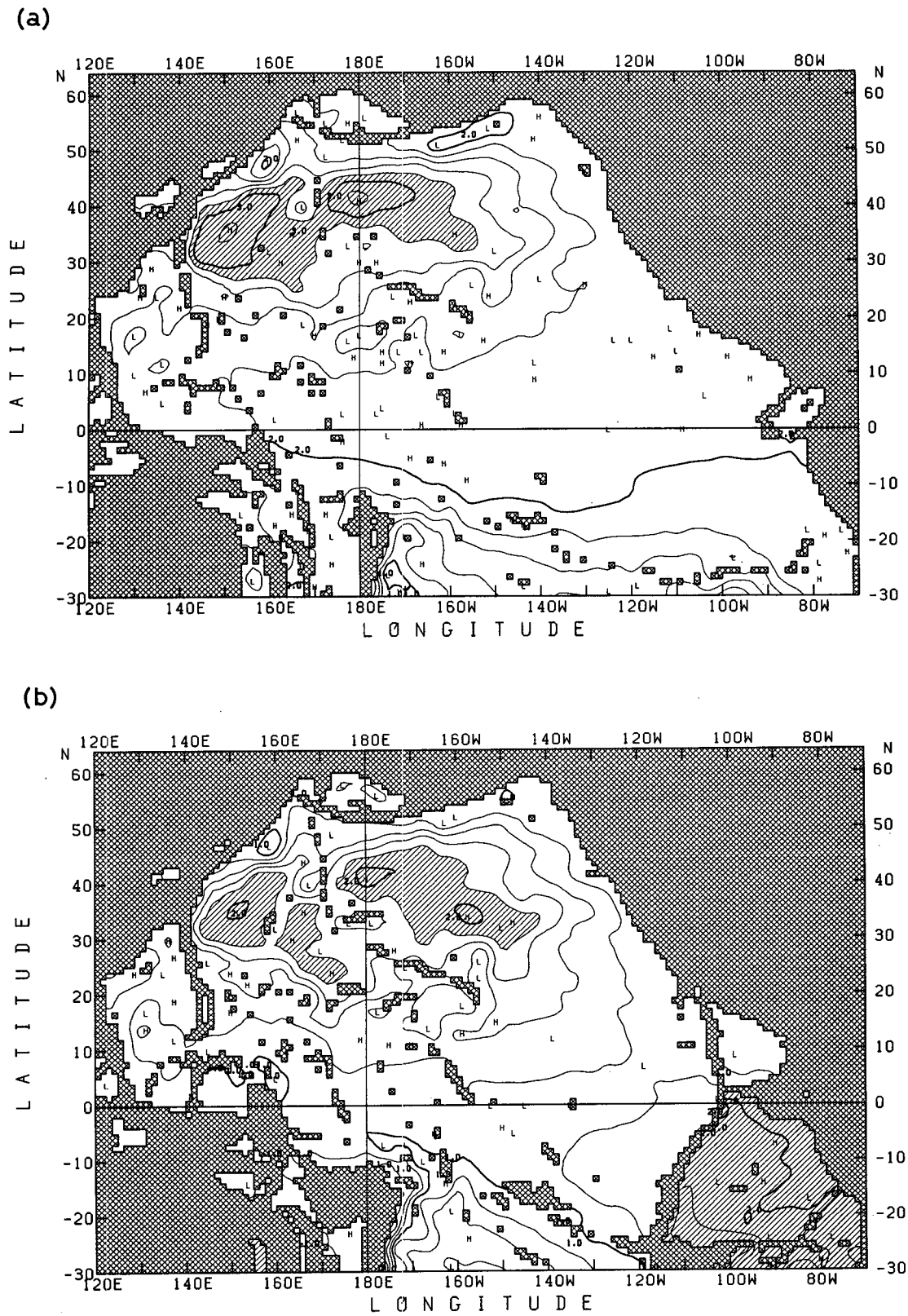

FIG. 3. Pressure field at (a) 2500 m, (b) 3500 m, and (c) 5000 m. Contour interval is 0.2 cm. Relatively high pressure regions are hatched.

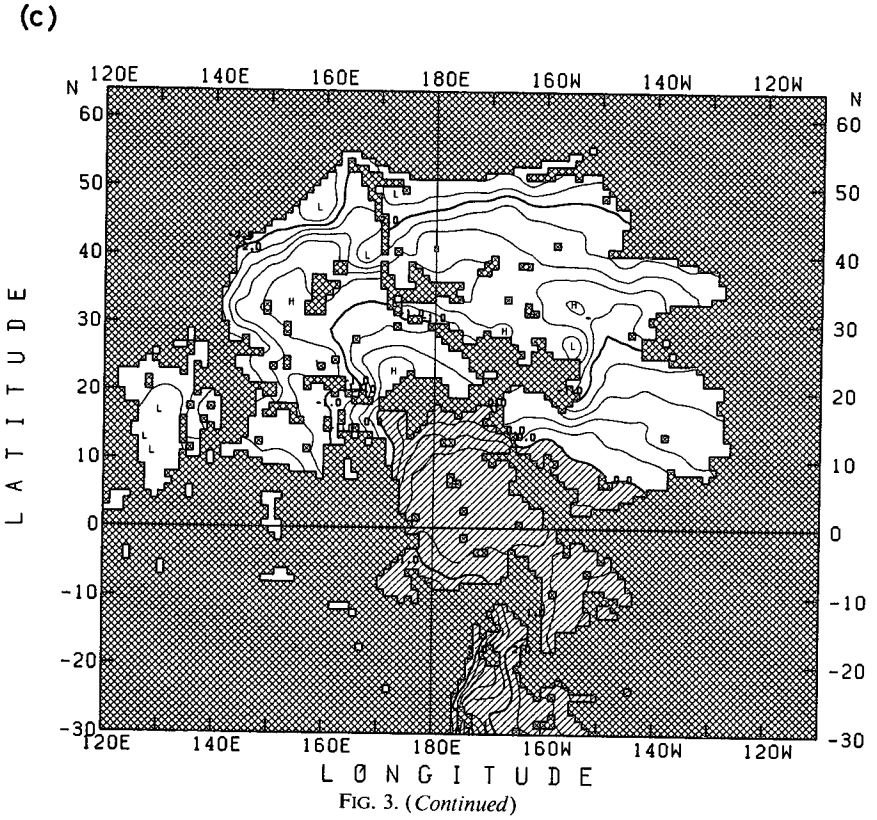

FIG. 3. (*Continued*)

eastward current appear again at the northern margin of the North Pacific, but westward flow is dominant in the low-latitude band between the equator and 10°N.

The overall circulation pattern in the upper deep layer between 1750 m and 3250 m (Fig. 3a) also shows that the whole North Pacific is dominated by a single anticyclonic gyre. But in this layer there is a southward flow from the North to the South Pacific found at about 160°E (Fig. 2). This circulation pattern can be regarded as a "reversed" pattern of the Stommel–Arons circulation induced by the general vertical shrinking of the water column owing to the outflow. The western boundary stagnation (separation) point is around 20°N. The existence of the Philippine Sea somewhat modifies the pattern, a part of the southward western boundary flow elongated in the Philippine Sea.

4. Theoretical consideration

The present model result contradicts the Stommel–Arons flat-bottom circulation (Fig. 1 of Part I). The horizontal distribution of vertical velocity w allows insight into this discrepancy (Fig. 4). As expected from the meridional circulation (Fig. 2), at 3750 m positive w is dominant over the whole North Pacific, and negative values of w are confined to regions near bottom topography (Fig. 4a). This is also the case for the w distribution at 4250 m, that is, one level lower (not shown here).

Taking the finite difference between the two levels (Fig. 4b) reveals that negative values of dw/dZ are dominant in a wide area of the entire North Pacific, particularly, in most of the northeast and the central Pacific Basins, in spite of a northward inflow across the equator at this level (Fig. 2). Positive values are associated with the northward velocity component, as expected by the Sverdrup relation. These figures suggest that a water column at these levels generally upwells but may vertically shrink in the mean.

Figure 5 shows the vertical distributions of horizontally averaged w (W) and vertical transport (T), which are associated with the large-scale dynamics over the North Pacific north of 2.5°N. In this calculation, extreme values of w confined to local bottom topography were excluded because they do not contribute to the large-scale dynamics at the in situ level. Instead, those transports may contribute to it at other layers as lateral influxes or outfluxes to those layers. For example, in the situation where dense water enters a basin crossing over a sill, it first descends immediately after crossing the sill, and then spreads and ascends gradually in the remaining wide area of the basin. In this case, w simply averaged over the basin is zero below the sill depth, but a large-scale basinwide circulation may be formed

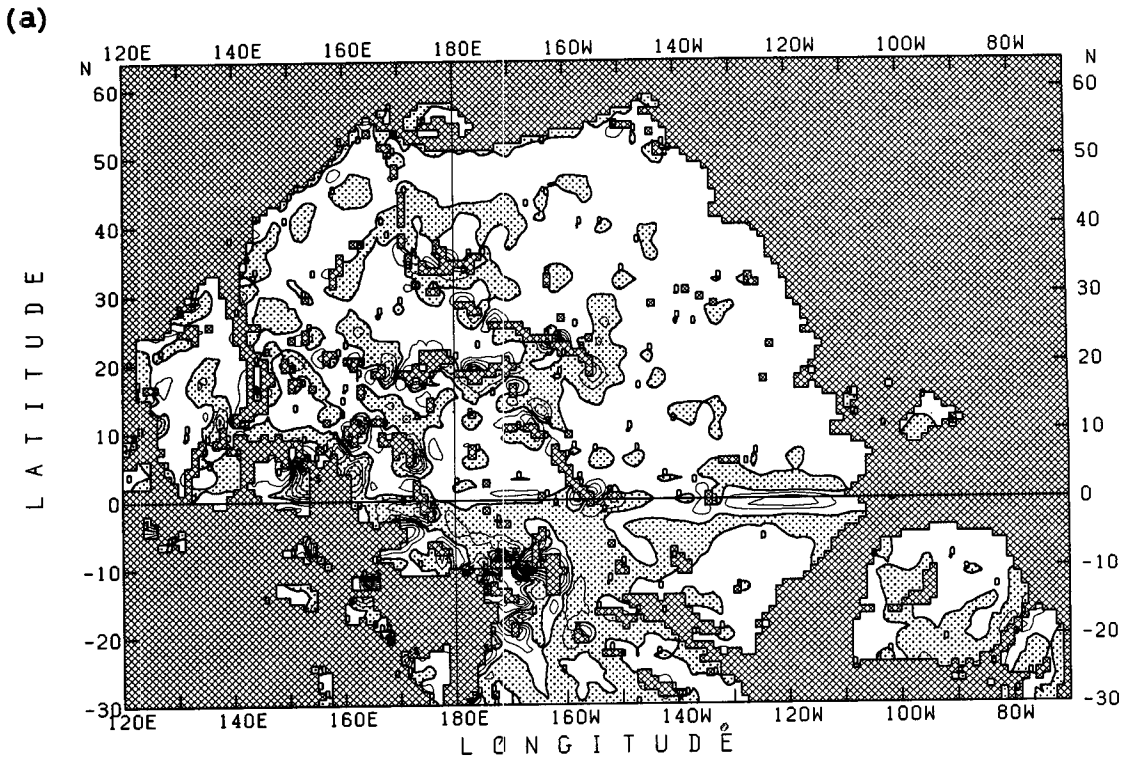

FIG. 4. (a) Horizontal distribution of vertical velocity at 3750 m, and (b) dw/dZ between 3750 m and 4250 m. Contour interval is 1×10^{-4} cm s^{-1} for (a) and 2×10^{-9} s^{-1} for (b). The shaded area corresponds to negative values of w or dw/dZ.

by the upwelling water. Only the upwelling water contributes to the large-scale dynamics in the layer below the sill depth, and the descending water in the narrow region near the sill works as a lateral influx to the layer. Thus, we excluded from the integration extreme 20% of w values (lowest 10% and highest 10%), in order to evaluate the vertical velocity and transport related to the large-scale dynamics (solid lines in Fig. 5). The broken lines show W and T estimated by including such extreme values (simple integration), and the horizontal bars indicate the ranges of those values obtained by increasing the exclusion rate from 10% to 30%. There is an arbitrariness in determination of the range of w values, but even a small exclusion rate (10%) leads to large differences in W and T below 3500 m, indicating that the simple integration (broken lines) underestimates interior W and T at those depths.

The W value thus obtained (solid line in Fig. 5a) is positive at every level, but the depth range in which a water column stretches ($dT/dZ > 0$) is confined to the deepest layer. The stretching, furthermore, is relatively weak, in spite of the abrupt increase of the vertical transport T in that layer. In the layer between 4250 m and 3750 m, T slightly increases but W decreases, as is expected from Fig. 4b.

These facts suggest an effect of the bottom topography on the flow field. Let us consider a layer in a basin with bottom topography (Fig. 6). The cross-sectional area is greater at the upper boundary than at the lower boundary. We assume that there is an upward vertical mass transport through this layer, and that the vertical velocity is horizontally homogeneous at each level. Then W is greater at the lower boundary than at the upper boundary because of the difference in area. That is, a water column generally upwells but vertically shrinks, and therefore, the interior flow has a southward component, provided that the Sverdrup relation $\beta v = f\,dw/dZ$ holds. This, in turn, means a northward western boundary current to compensate the interior flow, resulting in an anticyclonic gyre. This "hypsometric effect" has been discussed by Rhines and MacCready (1989) for f-plane dynamics. They demonstrated by a laboratory experiment that an anticyclonic circulation is generated in a bowl-shaped basin by the injection of dense water into the basin at its deepest level.

Figure 7 shows the vertical distribution of horizontal cross-sectional area of the North Pacific without the Philippine Sea based on the $5' \times 5'$ depth data by NODC. The area increases almost linearly in the abyssal layer between the 6000-m and 4000-m levels. This distribution is mainly owing to general westward deepening of the bottom depth and the gentle slope of the western flank of the East Pacific Rise (Fig. 1). Large-

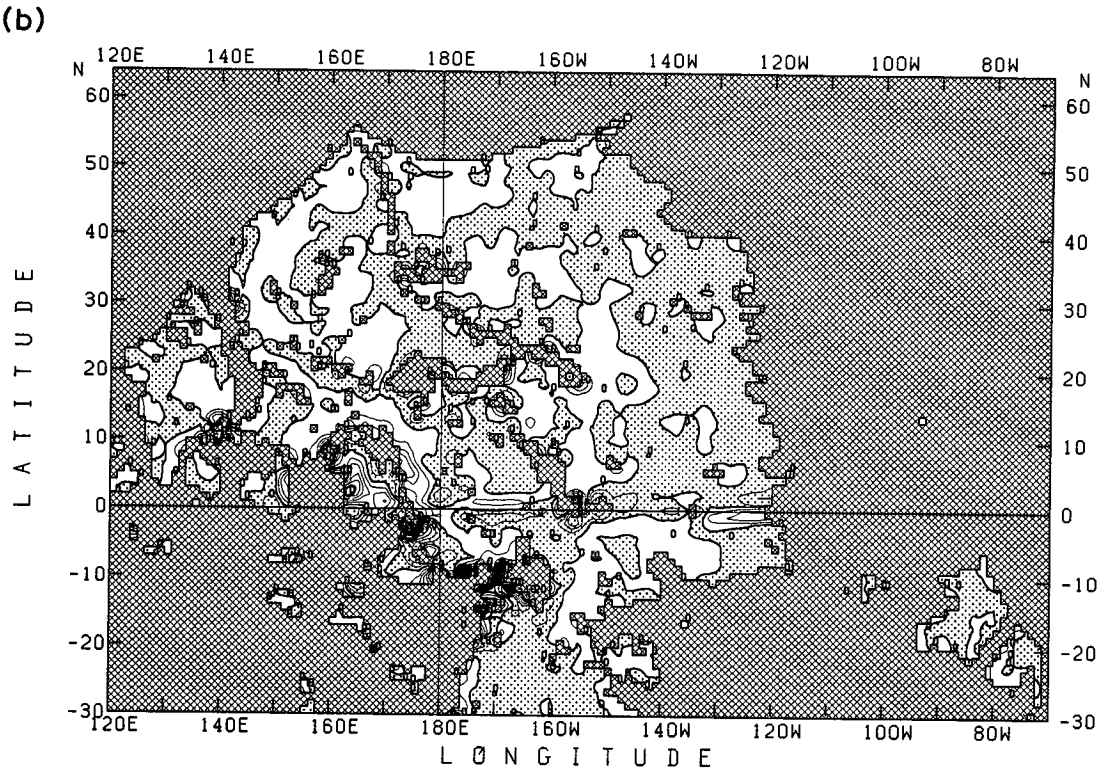

FIG. 4. (*Continued*)

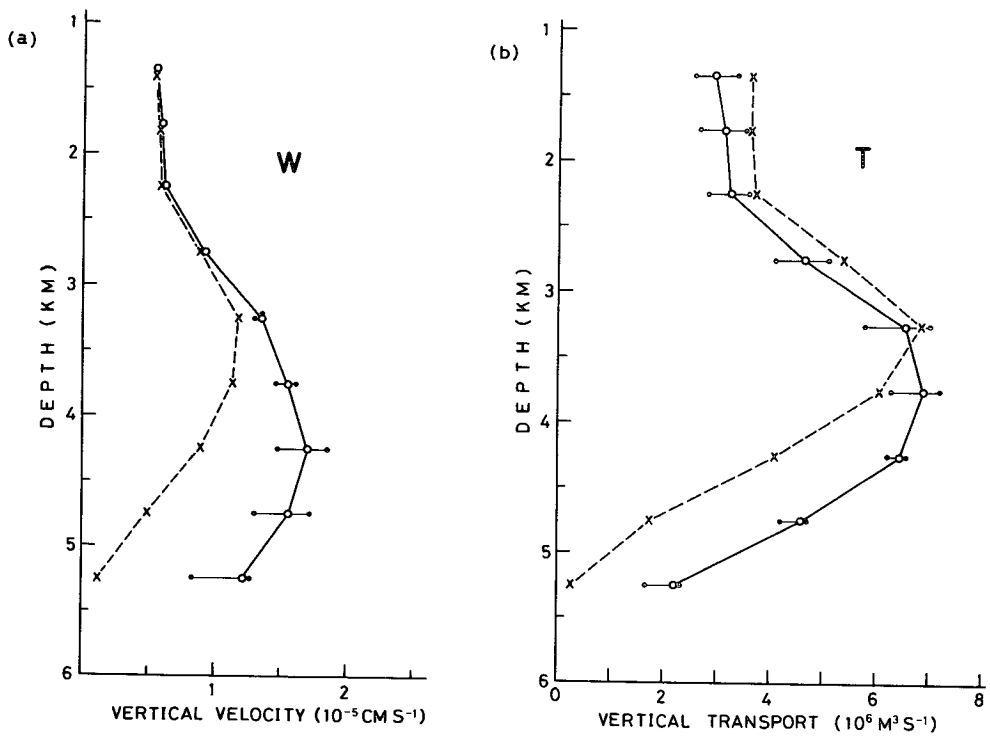

FIG. 5. (a) Vertical distributions of vertical velocity averaged over the North Pacific north of 2.5°N excluding 20% extreme values of w (solid line) and including the extreme values (broken line). See text for the horizontal bars. (b) Same as (a) but for the vertical transport.

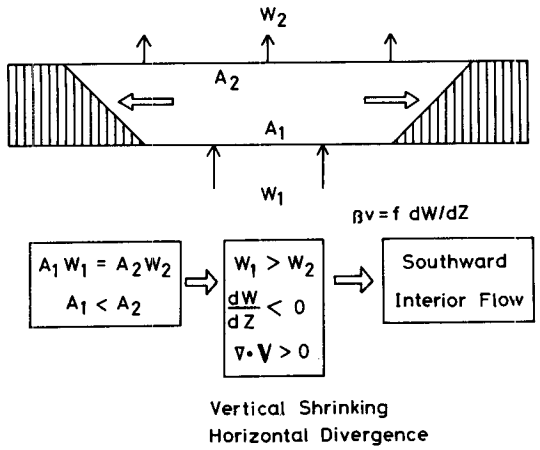

FIG. 6. Schematic of the "hypsometric effect."

scale seamount ridges also contribute to the distribution.

We formulate a conceptual model following Rhines and MacCready (1989). First we define some variables:

$S(Z)$: lateral influx or outflux of water mass at level Z,

$T(Z)$: total vertical mass transport through level Z,

$A(Z)$: horizontal cross-sectional area of the basin at level Z, and

$W(Z)$: horizontally averaged vertical velocity at level Z.

Then, the following relationships are satisfied:

$$T(Z) = \int_{-H}^{Z} S(Z')dZ' \quad \text{or} \quad S(Z) = \frac{dT(Z)}{dZ}, \quad (1)$$

$$W(Z) = \frac{T(Z)}{A(Z)}, \quad \text{and} \quad (2)$$

$$\frac{dW}{dZ} = -\frac{T}{A^2}\frac{dA}{dZ} + \frac{1}{A}\frac{dT}{dZ} = -\frac{W}{A}\frac{dA}{dZ} + \frac{S}{A}. \quad (3)$$

That is, $T(Z)$ is expressed as an integration of $S(Z)$ from the deepest bottom level $-H$ to level Z [Eq. (1)]; W is T divided by A [Eq. (2)] and dW/dZ is expressed by (3). The first term in (3) includes the vertical variation of cross-sectional area and is generally negative if W is positive, the hypsometry term following Rhines and MacCready (1989). The second term includes the lateral influx S, and we call this term the influx term. The sign of this term depends on the sign of S and influx is defined as positive. If the bottom is flat, the first term disappears, and further if S is a positive constant, then the flow should reduce to the Stommel–Arons circulation.

Next we estimate magnitudes of the two terms on the rhs of (3) for the North Pacific based on the model results. Figure 8a shows their vertical distributions together with dW/dZ, calculated by using W and T without 20% extreme values of w as shown by the solid lines in Fig. 5. The lateral influx $S(Z)$ is estimated by the latter form of (1), and contains not only purely horizontal influx crossing the equator at level Z, but also those redistributed by bottom topography as stated before. The hypsometry term is negative and large in magnitude in the deepest layer and monotonically decreases in magnitude upward. On the other hand, the influx term is large and positive in the deepest layer and negative in the shallower layer. As a result, in the deepest layer below the 4250-m level (the bottom layer), the two terms almost balance and dW/dZ is small in magnitude. This layer just corresponds to the layer in which the interior flow is essentially eastward (Fig. 3c). The relatively small positive value of dW/dZ in the bottom layer is owing to the northward western boundary flow, in which the Sverdrup relation also holds (Warren 1981). In the middle layer between the 4250-m and 3250-m levels (the lower deep layer), the influx term is small and dW/dZ is dominated by the hypsometry term. On the other hand, in the layer above the 3250-m level (the upper deep layer), the negative value of the influx term, that is, the outflux, dominates dW/dZ.

Figure 8b shows corresponding values of the three quantities based on the simply integrated W and T shown by the broken lines in Fig. 5. This process underestimates the magnitude of the hypsometry term in the bottom and lower deep layers, and overestimates the magnitude of the influx term in the lower deep layer, making the influx term dominant in both layers.

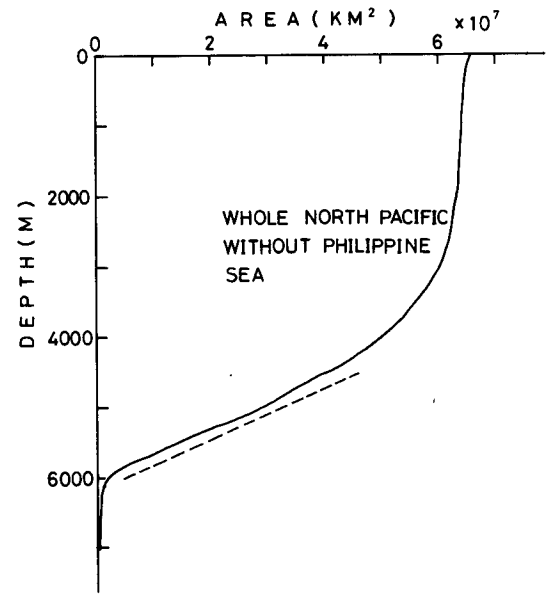

FIG. 7. Vertical distribution of cross-sectional area of the whole North Pacific without the Philippine Sea. The broken line is almost parallel.

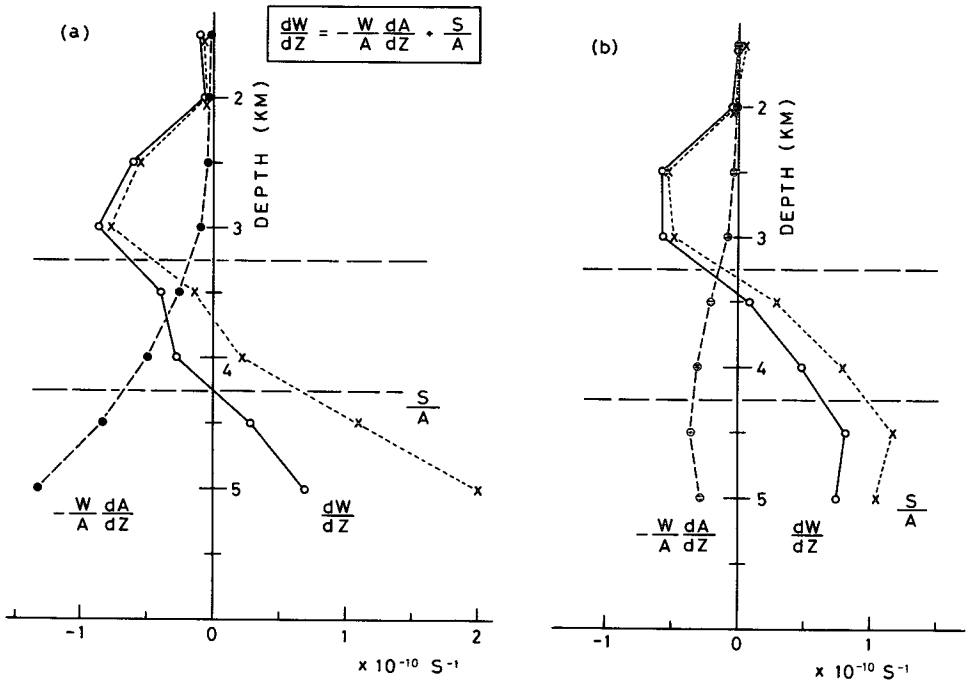

FIG. 8. (a) Vertical distributions of dW/dZ with its two components, the hypsometry term and the influx term, based on W and T estimated excluding 20% extreme values of w (solid lines in Fig. 5). (b) Same as (a) but obtained by W and T estimated including the extreme values of w (broken lines in Fig. 5).

This calculation cannot explain the simulated circulation patterns.

We draw schematic figures of the circulation based on the characteristics of these three layers (Fig. 9). In the bottom layer, the two terms of (3) almost balance, so that we assume $dW/dZ = 0$ in the interior region. Then, meridional velocity vanishes by the Sverdrup relation and the interior flow is due eastward (Fig. 9c). In the lower deep layer, dW/dZ is negative and $S = 0$, so there is only a single anticyclonic circulation (Fig. 9b). In the upper deep layer, dW/dZ is negative and S is negative; this is a reversed pattern of the Stommel–Arons circulation (Fig. 9a). These figures are qualitatively consistent with the corresponding horizontal circulation patterns shown in Fig. 3. The southward western boundary current in the upper deep layer (Fig. 9a) is elongated in the Philippine Sea as a cyclonic loop current, which we tentatively called the Circum-Philippine Sea Deep Current (Part I).

5. Conclusions

A theoretical rationale is given for the simulated abyssal circulation in the North Pacific Ocean. An analysis of the mean water column stretching (dW/dZ) reveals the importance of two competitive effects: hypsometry and lateral influx–outflux. The Stommel–Arons theory for the flat-bottom ocean circulation, which is based on the lateral influx–outflux alone, was modified by the introduction of realistic bathymetry. In the present case, this effect is present below 3250 m, that is, in the lower deep layer and the bottom layer. In the bottom layer, the cyclogenesis owing to the bottom water influx balances the hypsometry, resulting in eastward interior flow. In the lower deep layer the hypsometric effect dominates to make a single anticyclonic gyre over the entire North Pacific. An anticyclonic gyre in the upper deep layer is maintained by the vertical shrinking of the water column owing to the outflux from the North to the South Pacific.

Another effect of bottom topography on the large-scale dynamics is suggested: it may redistribute water mass fluxes, which work as lateral influxes or outfluxes at each layer. Extremely strong vertical flows near the topography do not contribute to the large-scale dynamics at their own levels, but they may contribute to it as lateral influx or outflux in other layers. This effect was determined by the fact that the dW/dZ analysis based on the vertical transport excluding extreme values of w well explains the simulated large-scale features, but a similar analysis based on the simply integrated vertical transport does not.

The determination of the range of w values that define W and T is somewhat arbitrary because there are no clear divisions in the frequency distribution of w values. But the present case has shown that the selection

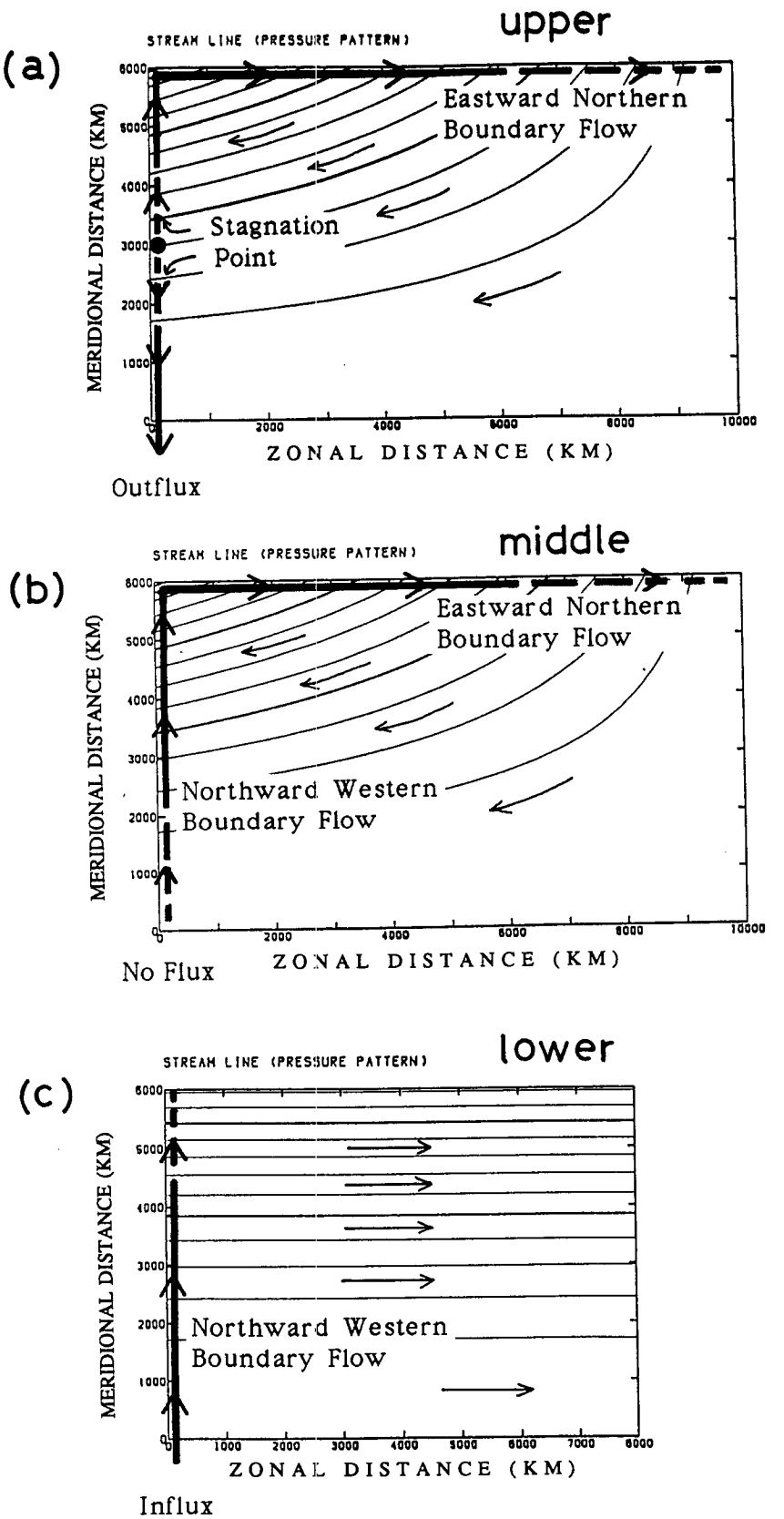

FIG. 9. Schematic figures of horizontal circulation patterns deduced by the vertical distribution of dW/dZ shown in Fig. 8a for (a) the upper, (b) the middle, and (c) the lower layer.

of a proper range of w values gives a consistent rationale for the simulated results.

Acknowledgments. The author thanks Drs. M. Endoh, T. Motoi, N. Yoshioka, and Y. Kitamura for very helpful discussions and comments. The author also expresses his gratitude to the reviewers for their critical and constructive comments and suggestions. This study was funded by the Meteorological Research Institute and also by the Japan WOCE program on the initiative of the Science and Technology Agency of Japan.

APPENDIX A

A New Definition of the Equation of State

The equation of state for sea water usually defines the density of sea water ρ in terms of in situ temperature T, salinity S, and pressure P (Fofonoff 1962; Friedrich and Levitus 1972; Bryan and Cox 1972; UNESCO 1981). But in numerical models the independent thermodynamical variables to be solved are not T and S, but potential temperature θ and S, so that a definition of the equation of state in terms of θ, S, and P is desired. Thus, we newly defined the equation of state in the same fashion as UNESCO (1981) using θ instead of T; that is,

$$\rho(S, \theta, P) = \rho(S, \theta, 0) \Big/ \left(1 - \frac{P}{K(S, \theta, P)}\right), \quad \text{(A1)}$$

where $K(S, \theta, P)$ is the secant bulk modulus. At the sea surface ($P = 0$), $\theta = T$, so we use the definition of $\rho(S, T, 0)$ in the UNESCO equation for $\rho(S, \theta, 0)$ in (A1). Then the problem is reduced to obtaining the formula of $K(S, \theta, P)$. We assume, as in the UNESCO equation,

$$K(S, \theta, P) = K_0(S, \theta) + A(S, \theta)P + B(S, \theta)P^2, \quad \text{(A2)}$$

where $K_0(S, \theta)$, $A(S, \theta)$, and $B(S, \theta)$ are polynomials of S and θ defined as follows:

$$K_0(S, \theta) = k_1 + k_2\theta + k_3\theta^2 + k_4\theta^3 + k_5\theta^4 + S(k_6 + k_7\theta + k_8\theta^2 + k_9\theta^3) + S^{3/2}(k_{10} + k_{11}\theta + k_{12}\theta^2), \quad \text{(A3)}$$

$$A(S, \theta) = a_1 + a_2\theta + a_3\theta^2 + a_4\theta^3 + S(a_5 + a_6\theta + a_7\theta^2) + S^{3/2}a_8 \quad \text{(A4)}$$

and

$$B(S, \theta) = b_1 + b_2\theta + b_3\theta^2 + S(b_4 + b_5\theta + b_6\theta^2). \quad \text{(A5)}$$

There are 26 unknowns: a_i (8), b_i (6), and k_i (12). In principle, we can also use the functional form of $K_0(S, T)$ in the UNESCO equation for $K_0(S, \theta)$ in (A2) for the same reason stated above, but we redefine $K_0(S, \theta)$ as well as $A(S, \theta)$ and $B(S, \theta)$ for the sake of better fitting. We determine the unknowns in the ranges of θ and S shown in Figs. A1 and A2, respectively. The pressure range is between 0 (surface) and 600 bar (6000 m). The ranges of θ and S contain those of Bryan and Cox (1972) for their definition of the equation of state and, therefore, more than 98% of sea water in the World Ocean falls in these ranges.

First, for every 10 bar, we give 41×41 pairs of θ and S in the ranges shown in Figs. A1 and A2. Next, for each set of (S, θ, P), in situ temperature T is calculated by Fofonoff's (1977) formula. In the formula, potential temperature Θ at an arbitrary reference pressure p_r of a sea water element having salinity s and in situ temperature t at pressure p_0 [i.e., $\Theta = \Theta(s, t, p_0 : p_r)$] is computed by integrating the adiabatic lapse rate and using a fourth-order Runge–Kutta integration algorithm. In our situation

$$T(S, \theta, P) = \Theta(S, \theta, 0 : P). \quad \text{(A6)}$$

Then, making use of the UNESCO equation, the density $\rho(S, T(S, \theta, P), P)$ is calculated. Finally, the 26 unknowns are determined by means of the least-squares method from the sets of (S, θ, P, ρ) $(41 \times 41 \times 60)$, using (A1) through (A5). Resulting values of the unknowns are as follows:

$k_1 = 19710.08$, $k_2 = 138.7224$, $k_3 = -1.490296$,
$k_4 = 6.070755 \times 10^{-3}$, $k_5 = -2.895094 \times 10^{-6}$,
$k_6 = 48.30427$, $k_7 = 0.1375978$,
$k_8 = -5.417062 \times 10^{-3}$, $k_9 = -2.027233 \times 10^{-5}$,
$k_{10} = 0.9166949$, $k_{11} = -4.043308 \times 10^{-2}$,
$k_{12} = 7.075453 \times 10^{-4}$, $a_1 = 3.375523$,
$a_2 = 2.236820 \times 10^{-2}$, $a_3 = -4.640599 \times 10^{-4}$,
$a_4 = 5.776355 \times 10^{-6}$, $a_5 = -9.777687 \times 10^{-3}$,
$a_6 = -1.535978 \times 10^{-4}$, $a_7 = 9.333798 \times 10^{-7}$,
$a_8 = 1.960003 \times 10^{-3}$, $b_1 = 2.015117 \times 10^{-4}$,

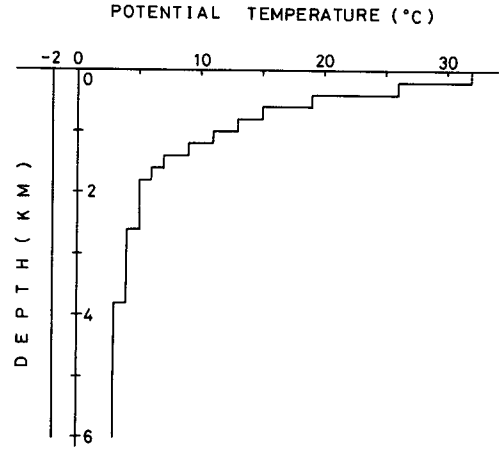

FIG. A1. Range of potential temperature θ, in which the equation of state is defined.

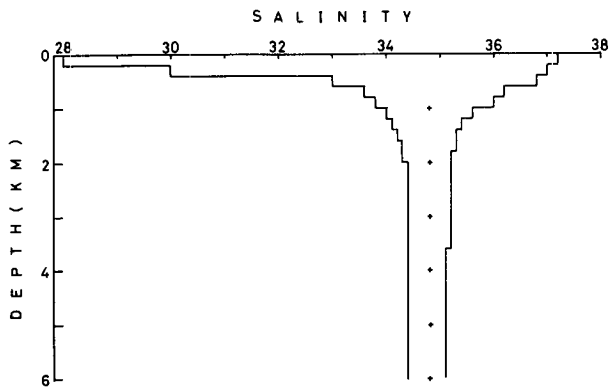

FIG. A2. Same as Fig. A1 but for salinity S.

$b_2 = -1.079882 \times 10^{-5}$, $b_3 = 3.237532 \times 10^{-7}$, $b_4 = -1.256429 \times 10^{-6}$, $b_5 = -9.601687 \times 10^{-9}$, and $b_6 = -1.129524 \times 10^{-9}$.

Values for checking the formula are $\rho(30, 25, 20) = 1020.42294$, $\rho(35, 5, 100) = 1032.24673$, and $\rho(35, 2, 600) = 1054.34495$.

Figure A3 shows standard difference and maximum difference in density values between those obtained by the present formula and by the UNESCO equation with Fofonoff's formula. These were calculated from the same pairs of (S, θ) $(N = 41 \times 41)$ at each pressure level, as was used to get the present formula. The maximum difference ranges from 10^{-5} to 3×10^{-4} kg m^{-3}, and this means its relative value ranges from 10^{-8} to 3×10^{-7}. The overall standard difference is 6.5×10^{-5} kg m^{-3}, that is, relatively 6.5×10^{-8}.

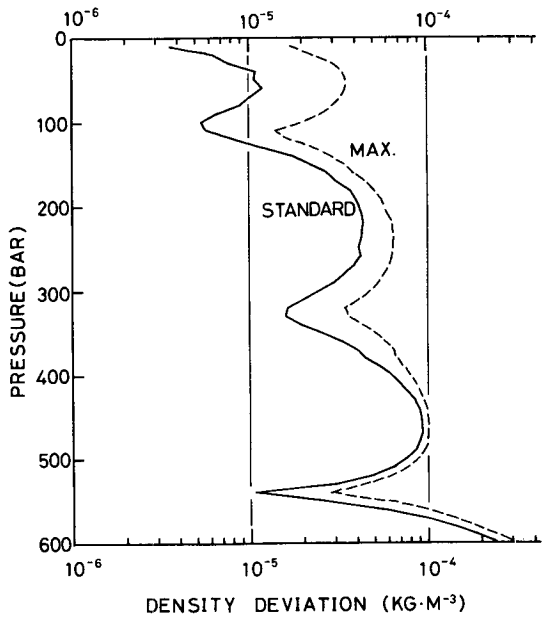

FIG. A3. Standard (solid line) and maximum (broken line) differences in density values between those obtained by the present formula and by the UNESCO equation with Fofonoff's formula.

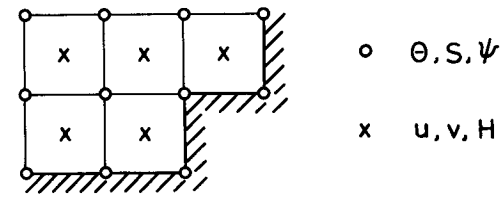

FIG. A4. Horizontal gridpoint alignment.

In the course of using Fofonoff's formula, the pressure increment was taken as small as 10 bar, so that the temperature error introduced by the use of the formula is at most on the order of 10^{-7} °C (Fofonoff 1977). An expected absolute density error owing to this temperature error in the formula of the UNESCO equation is on the order of 10^{-8} kg m^{-3} (UNESCO 1981). This value is much smaller than those in Fig. A3, and we can neglect the error introduced by the use of Fofonoff's formula.

According to Millero et al. (1980), the standard difference in specific volume between observed and calculated values (by the UNESCO equation) over the oceanic ranges of T, S, and P is 5.0×10^{-9} m^3 kg^{-1}. The difference is relatively 5.0×10^{-6}, and the relative difference in density should be identical to this value. Our relative standard difference value of 6.5×10^{-8} is two orders smaller than this value and even the relative maximum value of 3.0×10^{-7} is one order smaller. The present formula can be put to practical use not only in numerical experiments but also in data analyses.

APPENDIX B

Some Aspects of Modeling Technique

a. Mass conservation and vertical mass flux

The horizontal gridpoint alignment is shown in Fig. A4. Coastlines are defined by connecting grid points for potential temperature (θ), salinity (S), and transport streamfunction (Ψ). Velocity (u and v) is calculated at the center of four adjacent points for potential temperature, so that it is possible for water to flow through a one-grid channel. Depth (H) is defined at velocity points.

We define two kinds of mass conservation equations, for T–S boxes shown by broken lines in Fig. A5 and for U–V boxes shown by solid lines. The continuity equation for the T–S box (i, j) is defined as

$$\mathrm{MC}^T_{i,j} \equiv u^*_{i-1/2,j} - u^*_{i+1/2,j} + v^*_{i,j-1/2} - v^*_{i,j+1/2} + \mathrm{WF}^T_{i,j,k+1} - \mathrm{WF}^T_{i,j,k} = 0,$$

where

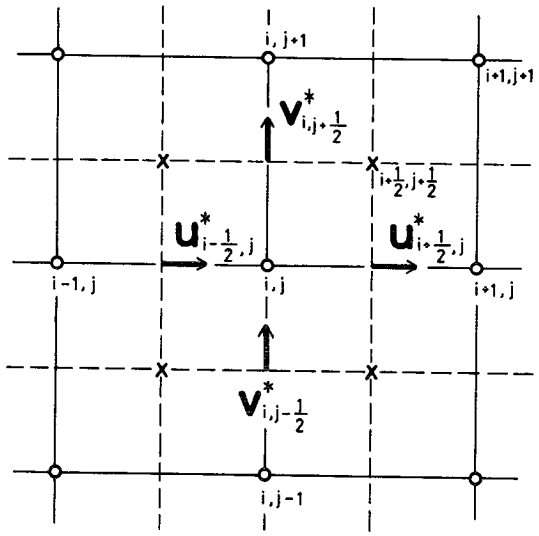

FIG. A5. Definition of mass fluxes u^*'s and v^*'s.

$$u^*_{i-1/2,j} = \frac{1}{2}\,(u_{i-1/2,j-1/2}\Delta Z_{i-1/2,j-1/2} + u_{i-1/2,j+1/2}\Delta Z_{i-1/2,j+1/2})\Delta Y,$$

$$v^*_{i,j-1/2} = \frac{1}{2}\,(v_{i-1/2,j-1/2}\Delta Z_{i-1/2,j-1/2} + v_{i+1/2,j-1/2}\Delta Z_{i+1/2,j-1/2})\Delta X,$$

and WF^T are vertical mass fluxes; ΔX, ΔY, and ΔZ are two horizontal and vertical grid intervals, respectively. If this layer touches the bottom, ΔZ is horizontally variable. The vertical suffix "$k + 1/2$" is omitted in the equations above. The boundary condition for $\mathrm{WF}^T_{i,j}$ is

$$\mathrm{WF}^T_{i,j} = 0$$

at the sea surface and bottom.

The mass conservation for the U–V box $(i + 1/2, j + 1/2)$ is derived from those for surrounding TS boxes (Ohnishi 1978):

$$\mathrm{MC}^U_{i+1/2,j+1/2} \equiv \frac{\mathrm{MC}^T_{i,j}}{N_{i,j}} + \frac{\mathrm{MC}^T_{i+1,j}}{N_{i+1,j}} + \frac{\mathrm{MC}^T_{i,j+1}}{N_{i,j+1}} + \frac{\mathrm{MC}^T_{i+1,j+1}}{N_{i+1,j+1}} = 0,$$

where $N_{i,j}$ is the number of sea boxes around the T–S point (i, j). As long as the U–V box concerned is sea, each of N's in the equation is not zero. Then, the vertical mass flux for the U–V box $(i + 1/2, j + 1/2)$, $\mathrm{WF}^U_{i+1/2,j+1/2}$, is defined by surrounding WF^T's as

$$\mathrm{WF}^U_{i+1/2,j+1/2} = \frac{\mathrm{WF}^T_{i,j}}{N_{i,j}} + \frac{\mathrm{WF}^T_{i+1,j}}{N_{i+1,j}} + \frac{\mathrm{WF}^T_{i,j+1}}{N_{i,j+1}} + \frac{\mathrm{WF}^T_{i+1,j+1}}{N_{i+1,j+1}}.$$

In this definition, $\mathrm{WF}^U_{i+1/2,j+1/2}$ at the bottom can have nonzero value if any one of the adjacent U–V boxes has greater layer number than that at $(i + 1/2, j + 1/2)$, naturally expressing oblique upward or downward flows along bottom slope.

Explicit specification of vertical velocity at the sloping bottom based on horizontal velocity and depth gradient, which seems to be a cause of computational instability at steep slopes in the GFDL scheme, is not made, so that smoothing of bottom depth is not required. This, in turn, leads to physically more accurate velocity field at depth, because it is sensitive to bottom topography. The scheme for such mass fluxes and momentum advection by those fluxes was developed by Ishizaki and Motoi (1994, unpublished manuscript), based on Takano (1978) and Ohnishi (1978), in a highly vectorized fashion.

b. Barotropic vorticity equation

The barotropic component of velocity is obtained by solving the vertically averaged vorticity equation with the iterative overrelaxation method. In our model domain, however, there are ten islands so that the region is multiconnected (Fig. 3 of Part I). In such a case, there are two ways to internally determine the values of transport streamfunction at inner boundaries: the hole relaxation method (Takano 1974), hereafter referred to as the H method; and Kamenkovich's method (Kamenkovich 1962), hereafter referred to as the K method. The latter was originally applied to solve a steady-state boundary value problem by Kamenkovich (1962) and developed to apply to an initial value problem by Bryan (1969). But recently, most model experiments make use of the H method (e.g., Semtner 1986a,b). However, Ishizaki (1989) compared the computational efficiency of the two methods and found that a modified K method is more efficient than the H method. In the K method, only the inhomogeneous component of streamfunction is solved by relaxation in each time step and it converges faster as the number of islands increases. This is because the inhomogeneous solution has a fixed value "zero" at every internal and external boundary, so that the inclusion of many islands leads to a strong constraint for the solution. The H method converges slowly as the number of islands increases. We use the K method, including isolated small islands such as Easter Island and Tahiti for faster convergence (Fig. 3 of Part I).

There are two definitions for vorticity of barotropic velocity in terms of streamfunction, the 5-point scheme and the 9-point scheme (Takano 1974). The 9-point scheme takes more computer time of each iteration than the 5-point scheme. However, the 9-point scheme converges faster than the 5-point scheme because the streamfunction at a point is more tightly connected with those at surrounding points in the 9-point scheme. Furthermore, the 9-point scheme is consistent with the definition of barotropic velocity in the Arakawa B

scheme, which we use (Fig. A4). We adopted the 9-point scheme.

c. *Convective adjustment*

A scheme for convective adjustment was also developed, although its principle is the same as of the "complete mixing" of Marotzke (1991). Judgment of the static stability between two arbitrary vertically adjacent points was made at the middle pressure level between the two points, not at the surface pressure level ($p = 0$). This is because the relationship between two density values corresponding to two pairs of potential temperature and salinity (one with high temperature and high salinity and the other with low temperature and low salinity) at a certain pressure level could be reversed at a different pressure level, so that the judgment should be made near the in situ pressure level. This subtly affects the formation of the bottom and deep waters in the model.

REFERENCES

Bryan, K., 1969: A numerical method for the study of the circulation of the World Ocean. *J. Comput. Phys.*, **4,** 347–376.

——, 1984: Accelerating the convergence to equilibrium of ocean climate models. *J. Phys. Oceanogr.*, **14,** 666–673.

——, and M. D. Cox, 1972: An approximate equation of state for numerical models of the ocean circulation. *J. Phys. Oceanogr.*, **2,** 510–514.

Fofonoff, N. P., 1962: Physical properties of sea water. *The Sea,* Vol. 1, Interscience, 3–30.

——, 1977: Computation of potential temperature of seawater for an arbitrary reference pressure. *Deep-Sea Res.*, **24,** 489–491.

Friedrich, H., and S. Levitus, 1972: An approximation to the equation of state for sea water, suitable for numerical ocean models. *J. Phys. Oceanogr.*, **2,** 514–517.

Hellerman, S., and M. Rosenstein, 1983: Normal monthly wind stress over the world ocean with error estimates. *J. Phys. Oceanogr.*, **13,** 1093–1104.

Ishizaki, H., 1989: Comparison of computational efficiency of hole relaxation and Kamenkovich's method in solving vorticity equations in multi-connected regions. *Pap. Meteor. Geophys.*, **40,** 103–114.

——, 1994: A simulation of the abyssal circulation in the North Pacific Ocean. Part I: Flow field and comparison with observations. *J. Phys. Oceanogr.*, **24,** 1921–1939

Kamenkovich, V. M., 1962: On the theory of the Antarctic Circular Current (in Russian). *Okeanologiya,* **56,** 245–301.

Levitus, S., 1982: *Climatological Atlas of the World Ocean.* NOAA Prof. Paper No. 13, U.S. Govt. Printing Office, Washington, DC, 173 pp.

Marotzke, J., 1991: Influence of convective adjustment on the stability of the thermohaline circulation. *J. Phys. Oceanogr.*, **21,** 903–907.

Millero, F. J., C.-T. Chen, A. Bradshaw, and K. Schleicher, 1980: A new high pressure equation of state for seawater. *Deep-Sea Res.*, **27,** 255–264.

Ohnishi, Y., 1978: Method of numerical studies: Marginal seas (in Japanese). *Oceanography as Environmental Science,* S. Horibe, Ed., Tokyo University Press, 246–271.

Rhines, P. B., and P. M. MacCready, 1989: Boundary control over the large-scale circulation. *Parameterization of Small-Scale Processes,* P. Mueller, Ed., Hawaii Institute of Geophysics Special Publication, University of Hawaii, Honolulu, 75–99.

Semtner, A. J., Jr., 1986a: History and methodology of modeling the circulation of the World Ocean. *Advanced Physical Oceanographic Numerical Modeling,* J. J. O'Brien, Ed., D. Reidel, 23–32.

——, 1986b: Finite-difference formulation of a World Ocean model. *Advanced Physical Oceanographic Numerical Modeling,* J. J. O'Brien, Ed., D. Reidel, 187–202.

——, and Y. Mintz, 1977: Numerical simulation of the Gulf Stream and mid-ocean eddies. *J. Phys. Oceanogr.*, **7,** 208–230.

Smith, S. M., and J. Mammerickx, 1980: General bathymetric maps of the oceans (GEBCO). 5th ed. Canadian Hydrographic Service, Ottawa, Canada.

Stommel, H., and A. B. Arons, 1960: On the abyssal circulation of the world ocean. I. Stationary planetary flow patterns on a sphere. *Deep-Sea Res.*, **6,** 140–154.

Takano, K., 1974: A general circulation model for the World Ocean. Dept. of Meteorology Tech. Rep. No. 8, University of California at Los Angeles, 47 pp.

——, 1978: Influences of ridges on deep and bottom flows. *Oceanography as Environmental Science* (in Japanese), S. Horibe, Ed., Tokyo University Press, 27–44.

UNESCO, 1981: Tenth report of the joint panel on oceanographic tables and standards. UNESCO Tech. Papers in Mar. Sci., No. 36, 25 pp.

Warren, B. A., 1981: Deep circulation of the World Ocean. *Evolution of Physical Oceanography: Scientific Survey in Honor of Henry Stommel,* B. A. Warren and C. Wunsch, Eds., The MIT Press, 6–41.